J Appl Electrochem (2009) 39:1279–1285
DOI 10.1007/s10800-009-9796-3

ORIGINAL PAPER

Effect of polarization type on properties of Ni–W nanocrystalline electrodeposits

S. Kabi · K. Raeissi · A. Saatchi

Received: 24 August 2008 / Accepted: 9 January 2009 / Published online: 28 January 2009

Abstract Nickel–tungsten nanocrystalline coatings were electrodeposited from a Watts type bath onto a copper substrate, at different current densities selected from activation, mixed and diffusion controlled regions in the cathodic scan plot at room temperature. The results confirm that tungsten codeposition proceeds via the adsorption and reduction of complexes produced in the bulk of solution. The coatings obtained were single phase solid solutions and their grain sizes increased with current density. A cauliflower-type surface morphology with highest hardness was obtained when the current density was in the activation controlled region. The surface morphology obtained in the mixed controlled region was distorted, and then converted to a nodular morphology in the diffusion controlled region. In the mixed control region, coatings with the highest corrosion resistance were obtained due to the lowest exchange current density for water reduction.

Keywords Ni–W · Coating · Electrodeposition · EIS · Nanocrystalline · Corrosion resistance

1 Introduction

Nickel–tungsten alloys are known for their excellent corrosion and wear resistance, high hardness and magnetic properties [1]. The electrodeposition of Ni–W alloys has been carried out from different baths using either dc or pulse plating techniques [2]. Some authors have found higher W in the deposits obtained by pulse as compared with dc technique at the same average current densities [2].

Many investigations have been devoted to electrodeposition of W with iron group metals. Yamasaki et al. [1] studied the formation of amorphous and nanocrystalline Ni–W alloy electrodeposits and found that the tungsten content of deposits is strongly influenced by ammonium chloride concentration in the plating bath. The X-ray diffraction peaks of the deposits obtained were broadened by increasing the tungsten percentage and an amorphous phase eventually appeared at a tungsten content of more than about 20 at.% [1]. A suitable electrolyte for electrodeposition of Ni–W alloys applicable for micro device fabrication is ammonia-citrate electrolyte used with and without carbonates. The electrolytes containing carbonates are more robust as the deposit composition is less sensitive to electrolyte pH and current density [3].

The effect of W on the mechanical properties of nanocrystalline Ni–W alloys has also been studied. Schuh et al. found that the hardness of Ni–W alloys is higher than that achievable in pure nanocrystalline Ni at the finest scale of 12–15 nm. The role of solid-solution strengthening was estimated from a standard theory, and found to be negligible compared with a very large effect of grain boundary strengthening in the nanocrystalline range [4]. Consequently, it is proposed that the improved hardness found in the Ni–W alloys arises primarily from their finer grain size [4].

The mechanism of W codeposition is not yet clear. Several hypotheses have been proposed about the induced codeposition of W with the iron group metals. Eliaz et al. [5] suggest that induced codeposition of W with the iron group metals can take place in five possible ways: (1) an intermediate oxide of W is formed which is subsequently reduced to the metal form by atomic

S. Kabi · K. Raeissi (✉) · A. Saatchi
Department of Materials Engineering, Isfahan University of Technology, Isfahan 84156-83111, Iran
e-mail: k_raeissi@cc.iut.ac.ir

hydrogen adsorbed on the freshly deposited iron-group metal that acts as a catalyst; (2) complex ions of W and the iron-group metal, which are formed in the electrolyte bulk, adsorb on the cathode surface and are reduced, thus allowing alloy deposition; (3) intermediate reaction species on the cathode surface subsequently decompose, providing the reduced form of W; (4) increasing the deposition potential of W results in the formation of a solid solution or intermetallic compound; (5) the activation polarization involved in the deposition of the inducing metal assists the codeposition of W.

In Ni–W electrodeposion, Younes et al. [6–8] found evidence of W deposition from mixed complexes such as $[(Ni)(WO_4)_2(H)_2(Cit)]^{2-}$ and $[(WO_4)(H)_n(Cit)]^{5-n}$. Obradovic et al. [9] state that $[WO_4HCit\ H_3]^{2-}$ complexes are electroactive and, due to their low concentration, W deposition is a diffusion controlled process. On the other hand, Ibrahim et al. [10] found that alloy formation in the Co–W system takes place through electrochemical reduction of tungstate ion to tungstate oxide or hydroxide and then chemical reduction of tungstate oxide to tungsten metal with hydrogen atoms attached to the freshly deposited cobalt.

The aim of the present work was to study the electrodeposition of Ni–W alloys by EIS, to clarify the mechanism of W codeposition, factors influencing W content, and morphology of the coatings. The corrosion resistance of the coatings and the determining factors were also investigated.

2 Experimental procedures

Copper was used as substrate as a disk of 0.85 cm^2 surface area. The substrates were mechanically polished up to 600 grade abrasive paper and then electropolished in a solution containing 65% phosphoric acid and 35% distilled water for 13–14 min. Ni–W alloy was electrodeposited from a typical Watts type bath at room temperature. The composition of the bath is shown in Table 1. The numbers of Coulombs passed were kept constant at 36 °C. This led to a coating thickness of about 13 μm. The coating thickness was also measured using the cross sections of coated specimens.

The Ni–W alloy was electrodeposited using a platinum wire as an anode with a saturated standard calomel electrode (SCE) as reference electrode. Using dilute ammonia or dilute sulfuric acid, the pH of the bath was controlled and adjusted at 7.5. In order to measure the impedances, an EG&G AC (model 1025) coupled with an E.G&G Potentiostat/Galvanostat (model 263A) was used. Variation of potential with current (log i) was recorded after 30 min immersion of the coatings in 3.5 wt.% NaCl solution at room temperature, using potentiostat and a standard corrosion cell with graphite counter electrodes and SCE as reference. The scan rate was 1 mV s^{-1}.

A Philips XL30 Scanning Electron Microscope (SEM) was used to study the coating morphology. The hardness measurements are from the surface of coatings and the reported value is the average of three measurements. The presence of W in the coatings was determined by EDS coupled with SEM. The grain size of the coatings was determined from X-ray patterns obtained by diffractometry (Philips X'pert). The grain size was calculated using the angular width of the nickel (111) peak at its Full-Width at Half Maximum (FWHM) in conjunction with the Scherrer equation [11] given at follows:

$$d = \frac{0.9 \times \lambda}{\beta \times \cos \alpha} \quad (1)$$

where λ, β and θ are the wavelength of CuKα (1.5406 Å), the integral width and the diffraction angle, respectively. The four-parameter Gaussian function was used for curve fitting analysis required for FWHM determination. Instrumental line broadening was also measured by a silicon standard specimen and corrected by the Gaussian–Cauchy equation [11].

3 Results and discussion

3.1 Selection of suitable current densities for electrodeposition

Various current densities for electrodeposition were selected from the cathodic polarization plot (Fig. 1). Three polarization regions—activation, mixed (activation + diffusion)

Table 1 Composition of the Watts bath and conditions for Ni–W electrodeposition

$NiSO_4 \cdot 6H_2O$	Ni source	0.046 M
$Na_2WO_4 \cdot 2H_2O$	W source	0.155 M
$Na_3C_6H_5O_7 \cdot 2H_2O$	Complexing agent	0.5 M
NH_4Cl	Improves faradic efficiency	0.5 M
NaBr	Improves conductivity	0.15 M
Bath temperature	…	298 K
pH	…	7.5
Current density	…	2.5,7.5,15,30,50 mA cm^{-2}

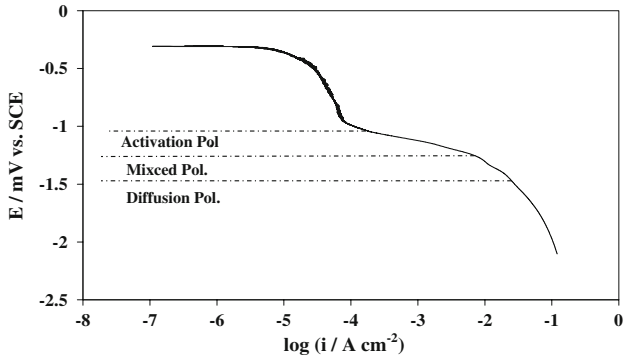

Fig. 1 Cathodic polarization plots of Ni–W deposition obtained in bath. (Scan Rate: 40 mV s^{-1})

and diffusion are seen in Fig. 1. Current densities of 2.5 mA cm^{-2} in the activation polarization region, 7.5 and 15 mA cm^{-2} in the mixed polarization region and 30 and 50 mA cm^{-2} in the diffusion region were selected for electrodeposition. These current densities correspond to potentials of −1050 to −1190, −1340 to −1480 and −1620 mV vs. SCE, respectively.

3.2 EIS investigation of Ni–W electrodeposition

In order to investigate the electrochemical aspects of Ni–W electrodeposition, EIS tests were performed at −1050, −1190, −1340, −1480 and 1620 mV. As mentioned above, these potentials correspond to current densities of 2.5, 7.5, 15, 30 and 50 mA cm^{-2}, respectively. Nyquist plots for Ni–W electrodeposition obtained at the above potentials are shown in Fig. 2. Three time constants can be distinguished on the Nyquist plots. The first, which appears as a small capacitive loop at high frequencies, should belong to the adsorption of complexes. The second, which appears as a capacitive loop at medium frequencies, is related to double layer capacitance parallel to charge transfer resistance. The third loop which appears as an inductive loop at −1050 mV (Fig. 2a), is most probably due to the relaxation of adsorbed electrochemical species during electrodeposition. As seen from Figs. 2b to 2e, by increasing the potential, the inductive loop is replaced by a second capacitive loop. This capacitive loop which appears at lower potentials is due to the slow bulk diffusion of electrochemical active species which participate in the electrodeposition process. These species are most probably the complex ions $[(WO_4)(H)n(Cit)]^{5-n}$, $[(Ni)(WO4)(H)(Cit)]^{-2}$ [6–8] and $[WO_4HCitH_3]^{2-}$ [9]. As mentioned before, deposition of W occurs only through reduction reactions which proceed through the production of complexes formed in the bulk solution. The concentration of the complexes is very low and this causes mass transport limitations [9].

Table 2 summarizes the corresponding values of charge transfer resistance (R_{ct}) and double layer capacitance (C_{dl}) extracted from the Nyquist plots in Fig. 2. The R_{ct} were obtained by direct fitting of a circle onto the high frequency capacitive loop. The diameter of this circle is considered as the R_{ct}. As seen in Fig. 3, the R_{ct} is reduced with decrease in cathodic potential. The decrease in R_{ct} may be related to the increase in surface diffusion of adions [12]. It has been proposed that a typical charge transfer takes place via three steps: ion transfer from the double layer to terrace sites and its adsorption, surface diffusion of adsorbed ions (adions) on terrace sites, and surface diffusion of adions on step-edge sites to the active sites for reduction [13]. It is well known that increasing the surface diffusion of adions facilitates their flux to the active growing sites and thus accelerates grain growth. Therefore, higher rates of grain growth, and thus larger grain size, are expected at lower cathodic potentials (i.e. higher current densities) [13].

3.3 Grain size determination and tungsten content

XRD patterns of the as-deposited Ni–W alloy coatings are shown in Fig. 4. From the patterns obtained, a solid solution of face-centered cubic structure is deduced for Ni–W coatings. Table 3 shows the grain size and W content of coatings obtained at different current densities. It has been shown that the grain size measured by the Gaussian–Cauchy equation is similar to that obtained by TEM observations [14, 15].

Results indicate that the as-deposited coatings consist of nanocrystalline grains. It is also shown that the grain size increases from 13.2 to 21.5 nm by increasing the current density from 2.5 to 50 mA cm^{-2} (Table 3). This is in accordance with the variation of R_{ct} as discussed in the previous section. The W content of the deposits initially fell with increasing current density from 2.5 to 7.5 mA cm^{-2}, but then increased slightly with increasing current density up to 30 mA cm^{-2}. The W content of the deposit decreased again with further increase in current density to 50 mA cm^{-2}. Therefore, a coating with a minimum content of 4.6 at.% W was obtained at 50 mA cm^{-2}. These results confirm the EIS results which indicate that in the diffusion controlled region in Ni–W deposition, a limitation exists for W deposition. At 50 mA cm^{-2} it can be assumed that W is deposited at the same rate as at 30 mA cm^{-2}. Thus nickel should deposit at a higher rate to compensate for the deficiency in reduction current. This results in a lower W percentage in the coating. It is interesting to note that similar variations are also observed in the double layer capacitance (C_{dl}) (Table 2). It is seen that the variation of W follows closely with that of $C_{dl,}$ as shown in Fig. 5. An increase in W content is in accordance with increase in C_{dl} and vice versa. It may be concluded that the complex ions, which adsorb instead of water molecules attached to the cathode surface, increase the capacitance at the cathode/

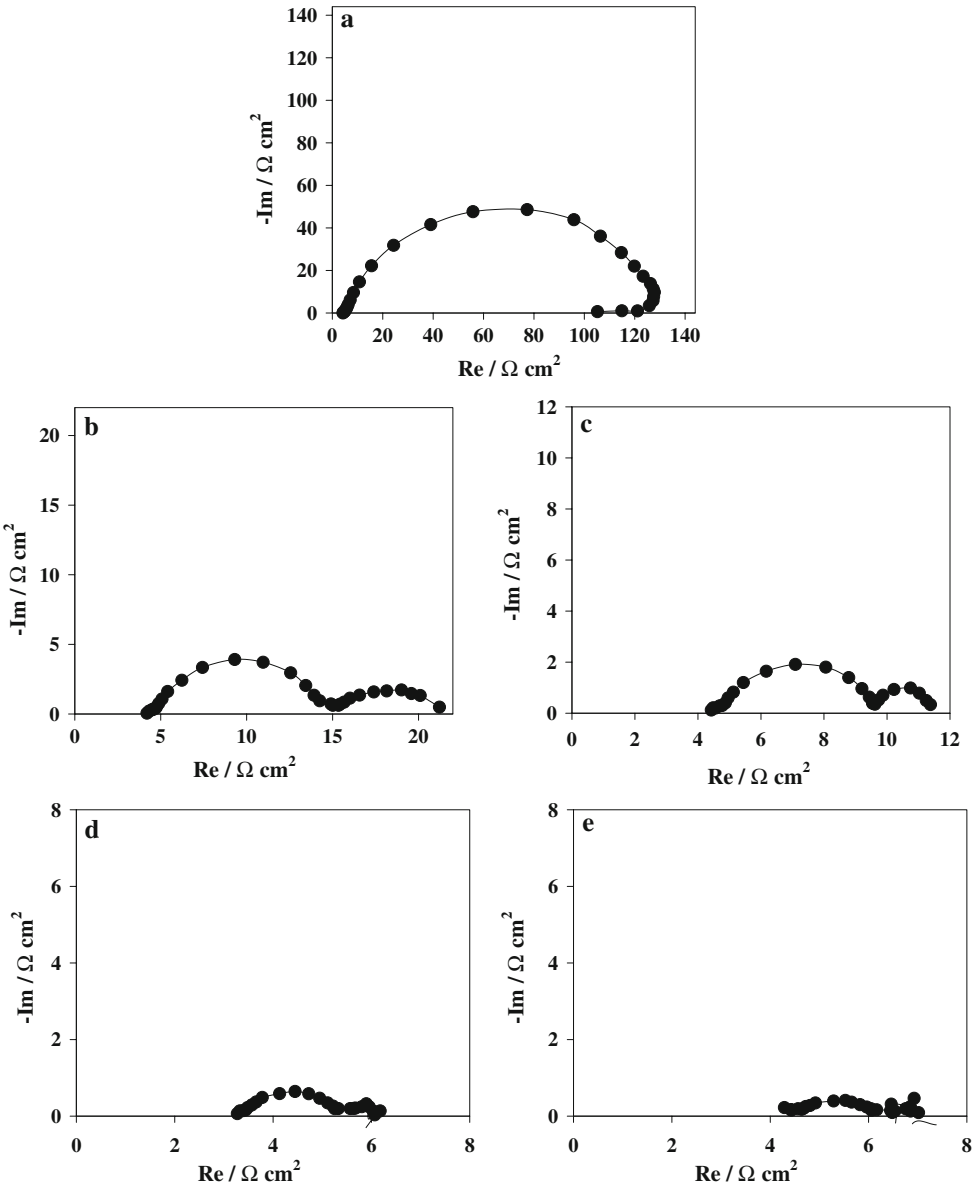

Fig. 2 Nyquist plots for Ni–W electrodeposition at (**a**) −1050, (**b**) −1190, (**c**) −1340, (**d**) −1480 and (**e**) −1620 mV

Table 2 C_{dl} and R_{ch} data extracted from Nyquist plots in Fig. 2

i (mA cm^{-2})	E (mV)	R_{ct} (Ω cm^2)	C_{dl} (μF cm^{-2})
2.5	−1050	128.7	376
7.5	−1240	10.01	143
15	−1340	5.03	164
30	−1480	2.758	299
50	−1620	2.234	106

electrolyte interface. This may be attributed to the electroactivity of such complexes [9].

Table 3 also shows the values of microhardness of the coatings. In Fig. 6, variation of microhardness is shown as

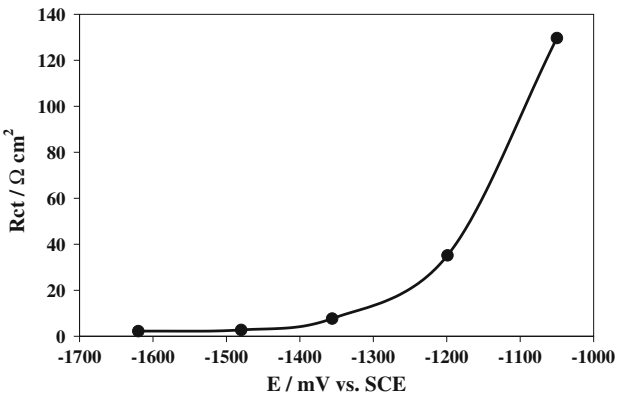

Fig. 3 Charge transfer resistance (Ω cm^2) versus cathodic potential

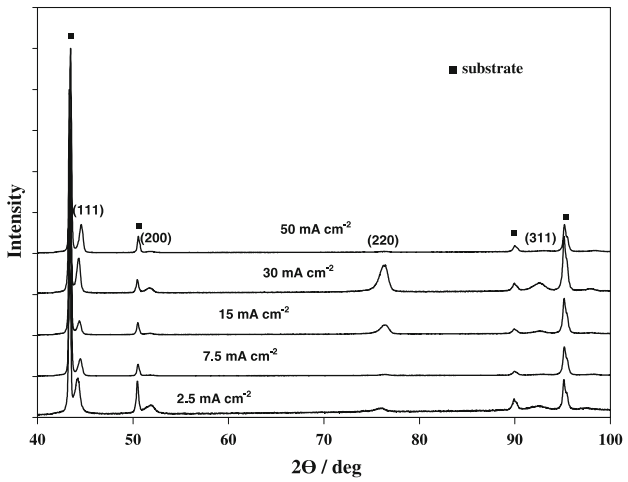

Fig. 4 XRD patterns of various Ni–W coatings

Table 3 Grain size, W content and microhardness of the coatings

i (mA cm^{-2})	E (mV)	W content (at.%)	Grain size (nm)	Microhardness (HV)
2.5	−1050	15.1	13.2	513.66 ± 30
7.5	−1240	7.5	17.3	420.66 ± 16
15	−1340	8.5	18.5	463.66 ± 20
30	−1480	9.1	19.8	478 ± 25
50	−1620	4.65	21.5	377.33 ± 26

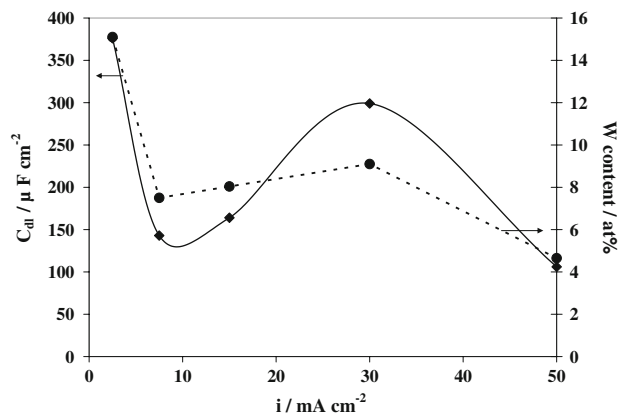

Fig. 5 Double layer capacitance (F cm^{-2}) and tungsten content (at.%) versus current density

a function of current density. The highest hardness was 514 HV, which was obtained for the coating produced at 2.5 mA cm^{-2} in the activation controlled region. Low magnitudes of hardness were obtained for the coatings electrodeposited at 30 and 50 mA cm^{-2} in the diffusion controlled region. As seen in Fig. 6, microhardness varies in a similar way as observed for W content in the coatings (Fig. 5). This confirms the role of W in increasing the hardness of nanocrystalline nickel alloy coatings. The

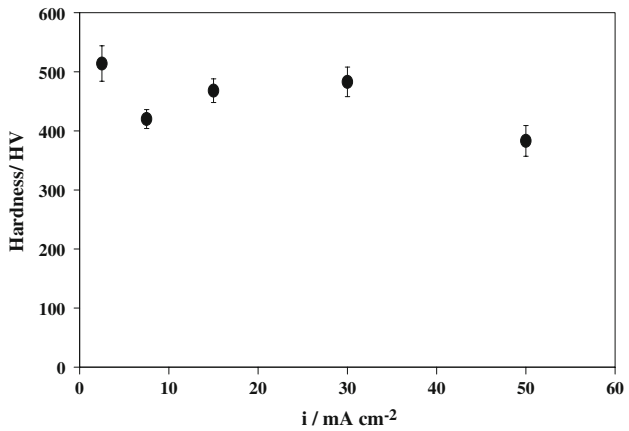

Fig. 6 Microhardness (HV) of the coatings obtaoined at different current density

effect of small variations in grain size obtained by increasing the current density on hardness also seems to be negligible.

Sriraman et al. [16] found a maximum hardness of 638HV for Ni–W coatings obtained from bath containing additive. Eliaz et al. [17] mentioned that the hardness of as-deposited Ni–W alloys at 30–70 °C is typically in the range 450–768 VHN.

3.4 Morphological observations

Figure 7 shows the SEM micrographs of the coatings produced at different current densities. A typical cauliflower-type surface morphology is obtained at 2.5 mA cm^{-2}. Increasing the current density resulted in semi distorted cauliflower morphology at 7.5 and 15 mA cm^{-2} in the mixed controlled region. Further increase in current density to 30 and 50 mA cm^{-2}, resulted in a completely different surface morphology which can be described as nodules. As seen in Fig. 7, this nodule-like morphology is obtained at current densities in the diffusion controlled region. Thus, it can be concluded that the morphology of Ni–W coatings depends strongly on the polarization type governing during the electrodeposition and does not show variations with W content or grain size. Mizushima et al. [18] and Miaomiao et al. [19] have also found similar morphologies in Ni–W systems.

3.5 Corrosion resistance evaluation

Figure 8 shows E vs. logi plots of the coatings obtained at various current densities. Passive film formation is evident. According to Sriraman et al. [20], tungsten preferentially migrates toward the surface of Ni–W coatings and forms oxides during the corrosion process.

Table 4 shows the related parameters extracted from E vs. logi plots in Fig. 8 using Tafel extrapolation. The

highest corrosion resistance (the lowest corrosion current density) is achieved for the coatings produced at 7.5 and 15 mA cm^{-2}. It should be mentioned that these current densities lie in the mixed controlled region (Fig. 1). Sriraman et al. have also found that the best corrosion resistance is for 7.54 at.% W in the coating which agrees with the results of the present study. The superior corrosion resistance of Ni–W alloy films is due to preferential dissolution of Ni and the formation of W rich film on the surface, which inhibits further corrosion [20].

In Table 4, the variation of intensity ratio of the most closed packed plane (111) to the intensity of the lowest closed packed plane (311) in nickel is also shown. This intensity ratio was calculated using the area of the corresponding peaks from X-ray patterns in Fig. 4. Since the most closed packed plane have the highest binding energy, it is expected that the coating with higher ratio of $I_{(111)}/I_{(311)}$

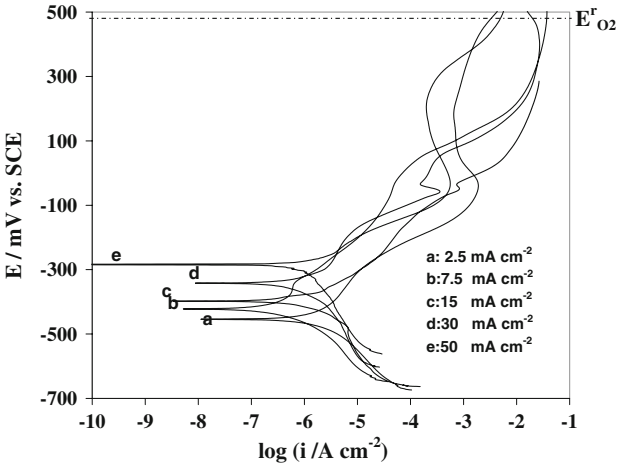

Fig. 8 E vs. logi plots of the Ni–W coatings

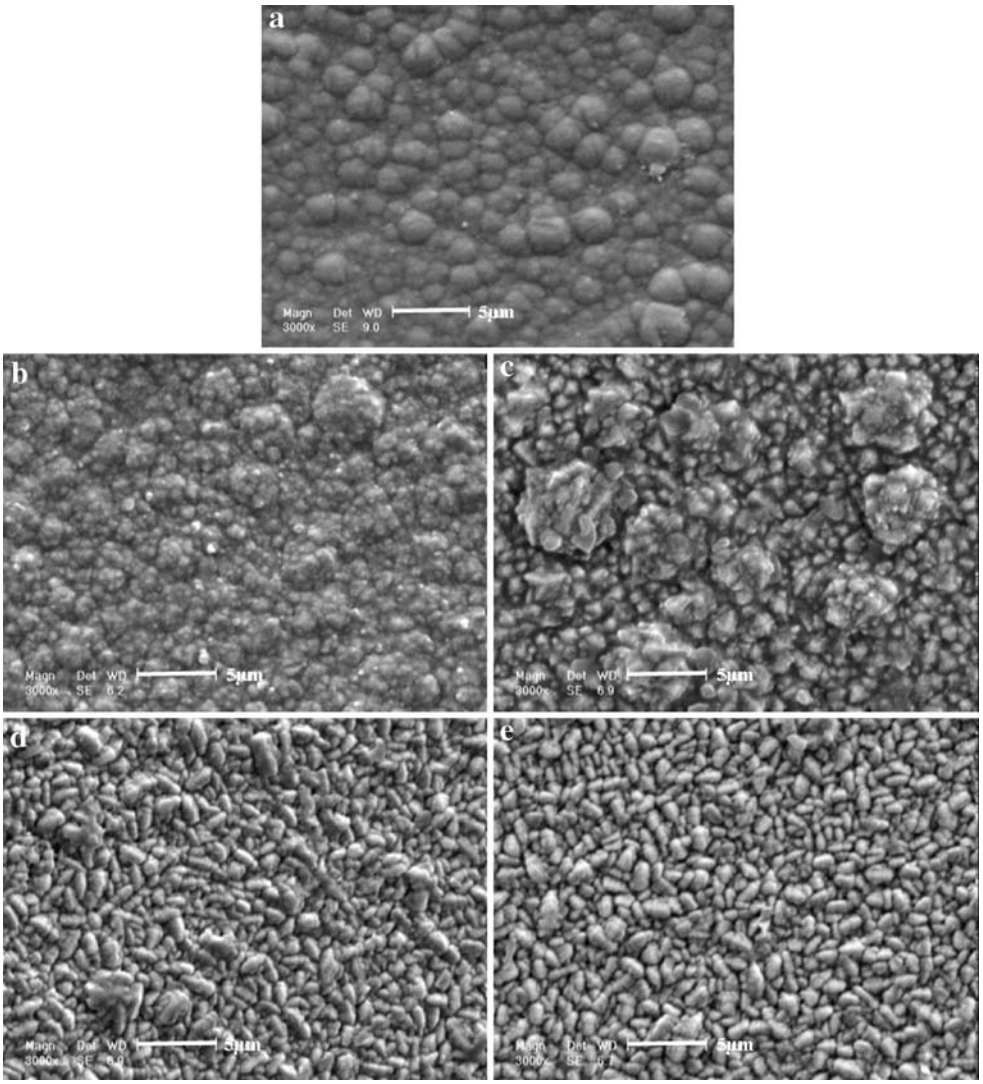

Fig. 7 SEM micrograph of Ni–W coatings produced at (**a**) 2.5, (**b**) 7.5, (**c**) 15, (**d**) 30 and (**e**) 50 mA cm^{-2}

Table 4 Extracted parameters from E vs. logi plots in Fig. 8

i (mA cm^{-2})	i_{corr} (μA cm^{-2})	E_{corr} (mV)	β_c (mV dec^{-1})	β_a (mV dec^{-1})	$I_{(111)}/I_{(311)}$	$\left(i_0^{H_2O}\right) \times 10^{-13}$ (mA cm^{-2})
2.5	4.4	−454	92	136	4.64	10
7.5	0.6	−422	138	–	10.93	2
15	1.7	−338	177	178	2.5	4
30	3.02	−342	194	151	1.83	7
50	3.7	−282	146	72	8.21	9

provides the higher corrosion resistance [21]. This phenomenon was not observed here. On the other hand, as seen from Table 4, the exchange current density of water reduction in the presence of oxygen $\left(i_0^{H_2O}\right)$ has its lowest value for coatings obtained in the mixed polarization region. This provides the lowest values of i_{corr} for these coatings. As seen in Table 4, the highest value of $\left(i_0^{H_2O}\right)$ (i.e. 10×10^{-13} mA cm^{-2}) is obtained for the coating produced at 2.5 mA cm^{-2}. It is concluded that the corrosion rate of nanocrystalline Ni–W coatings is proportional to the $\left(i_0^{H_2O}\right)$ on the coating which is most likely dependent on the morphology of the coating rather than the grain size or even W percentage.

4 Conclusion

1. The lowest grain size and highest percentage of W were obtained in the coating obtained in the activation controlled region of the polarization diagram. Accordingly, the lowest corrosion resistance was obtained for this coating.
2. The surface morphology of Ni–W coatings depends strongly on the polarization type involved during the electrodeposition and is neither related to the W content nor to the grain size.
3. The highest corrosion resistance was obtained for coatings produced in the mixed controlled region due to the lowest exchange current density of water reduction on the coatings.

References

1. Yamasaki T, Schlobmacher P, Ehrlich K, Ogino Y (1998) Nanostruct Mater 10:375
2. Obradovic MD, Bosnjakov GZ, Stevanovic RML, Maksimovic MD, Despic AR (2006) Surf Coat Technol 200:4201
3. Cesiulis H, Podlaha Murphy EJ (2003) Mat Sci 9:329
4. Schuh CA, Nieh TG, Iwasaki H (2003) Acta Mater 51:431
5. Eliaz N, Gileadi E (2006) Induced codeposition of alloys. Meeting of the Electrochemical Society No. 209, USA
6. Younes O, Zhu L, Rosenberg Y, Shacham Diamand Y, Gileadi E (2001) Langmuir 17:8270
7. Younes O, Gileadi E (2000) Electrochem Solid State Lett 3:12
8. Younes O, Zhu L, Gileadi E (2003) Electrochim Acta 48:2551
9. Obradovic MD, Bosnjakovb GZ, Despic AR, Stevanovic RML, Maksimovic MD (2003) J Electroanal Chem 552:185
10. Ibrahim MAM, Abdelrehim SS, Moussa SO (2003) J Appl Electrochem 33:627
11. Cullity BD, Stock SR, Stock S (2001) Elements of X-ray diffraction. Addison-Wesley, London
12. Wang L, Gao Y, Xu T, Xue Q (2006) Mater Chem Phys 99:96
13. Hassani SH, Raeissi K, Golozar MA (2008) J Appl Electrochem 38:689
14. Wang L, Zhang J, Gao Y, Xue Q, Hu L, Xu T (2006) Scripta Mater 55:657
15. Wu BYC (2002) Synthesis and characterization of nanocrystalline alloys in the binary Ni–Co system. M.Sc. thesis, University of Toronto
16. Sriraman KR, Ganesh Sundara Raman S, Seshadri SK (2006) Mat Sci Eng 418:303
17. Eliaza N, Sridhara TM, Gileadi E (2005) Electrochim Acta 50:2893
18. Mizushim Io, Tang PT, Hansen HN, Somers MAJ (2005) Electrochim Acta 51:888
19. Miaomiao MA, Donepudi VS, Sandi G, Sunc YK, Prakash J (2004) Electrochim Acta 49:4411
20. Sriraman KR, Ganesh Sundara Raman S, Seshadri SK (2007) Mat Sci Eng 460:39
21. Park H, Szpunar JA (1998) Corros Sci 40:525